Dalton Transactions

PAPER

View Article Online
View Journal | View Issue

Cite this: *Dalton Trans.*, 2016, **45**, 18241

Different manifestations of enhanced π-acceptor ligation at every redox level of $[Os(9\text{-}OP)L_2]^n$, n = 2+, +, 0, − (9-OP$^-$ = 9-oxidophenalenone and L = bpy or pap)†

Arijit Singha Hazari,[a] Alexa Paretzki,[b] Jan Fiedler,[c] Stanislav Zalis,[c] Wolfgang Kaim*[b] and Goutam Kumar Lahiri*[a]

Received 28th September 2016,
Accepted 14th October 2016

DOI: 10.1039/c6dt03764j

www.rsc.org/dalton

The title complexes were isolated as structurally characterised compounds $[Os^{II}(9\text{-}OP)L_2]ClO_4$, L = 2,2′-bipyridine (bpy) or 2-phenylazopyridine (pap), and were compared with ruthenium analogues. A reversible one-electron oxidation and up to three reduction processes were observed by voltammetry (CV, DPV) and spectroelectrochemistry (UV-vis-NIR, partially EPR). Supporting calculations (DFT, TD-DFT) were used to assess the oxidation state combinations of the different redox active ligands and of the metal, revealing the effects of Os *versus* Ru exchange and of bpy *versus* pap acceptor ligation. Several unexpected consequences of these variations were observed for members of the new osmium-containing redox series. Remarkably, the EPR results exhibit a clear dichotomy between the complex ion $[Os^{III}(9\text{-}OP^-)(bpy)_2]^{2+}$ and the radical species $[Os^{II}(9\text{-}OP^{\bullet})(pap)_2]^{2+}$, which has not been similarly observed for the analogous $[Ru^{III}(9\text{-}OP^-)L_2]^{2+}$ systems. This difference, unprecedented for $5d^n$ systems, is attributed to the superior stabilisation of the Os^{II} state by the strongly π-accepting pap ligands. The reduced forms $[Os^{II}(9\text{-}OP^-)(pap^{\bullet-})(pap)]$ and $[Os^{II}(9\text{-}OP^-)(pap^{\bullet-})_2]^-$ exhibit strong inter-ligand interactions, leading to spin isomers and electron hopping.

Introduction

9-Oxidophenalenone (9-OP$^-$, **A**), a special β-diketonate chelate ligand, has been studied with respect to its formation of a dianionic radical (**B**) *via* reduction. Complexes of a 9-oxidophenalenone anion or a dianion have been described with positively charged main group ions such Be^{2+}, B^{3+}, Al^{3+}, Si^{4+} and Ge^{4+}.[1] Our earlier research on ruthenium complexes $[Ru(9\text{-}OP)_n(L)_{3-n}]^m$ has provided evidence that both the transition metal and $(9\text{-}OP)^x$ can exhibit redox reactivity,[2] the latter with the formation of a dianionic (**B**) or also of a neutral radical (**C**). The $(9\text{-}OP)^x$ system may thus be included in the group of redox-active and potentially "non-innocent" ligands,[3] involving a rather uncommon situation[4] with six-membered chelate rings. Recently, Mandal *et al.* have reported iron(III) complexes $[Fe(9\text{-}OP)_3]^x$ and their functioning as electroactive materials for H_2O_2 fuel cell application.[5]

To complement the series with group 8 metals, we are now describing two osmium compounds [**1**]ClO_4 and [**2**]ClO_4 (Scheme 2) in contrast to the ruthenium analogues $[Ru(9\text{-}OP)(bpy)_2]ClO_4$ ([**3**]ClO_4)[2a] and $[Ru(9\text{-}OP)(pap)_2]ClO_4$ ([**4**]ClO_4).[2b] While the corresponding osmium and ruthenium compounds are frequently similar, there are distinct differences in certain complexes such as mixed-valent materials.[6,7] In comparison to ruthenium, osmium has a preference for higher oxidation states (lower redox potentials) and larger spin–orbit coupling parameters, manifest through the absorption spectral and magnetic effects (EPR g factors, spin–spin coupling).[6,7]

It is shown in this contribution that the contrast between complexes $\mathbf{1}^n$ with the moderate π-acceptor bpy and system $\mathbf{2}^n$ with the much stronger π-accepting[2a,b] pap can result in frequently variable oxidation state situations involving $(9\text{-}OP)^x$ and the metal in their respective accessible charge states.

[a]*Department of Chemistry, Indian Institute of Technology Bombay, Powai, Mumbai 400076, India. E-mail: lahiri@chem.iitb.ac.in*
[b]*Institut für Anorganische Chemie, Universität Stuttgart, Pfaffenwaldring 55, D-70550 Stuttgart, Germany. E-mail: kaim@iac.uni-stuttgart.de*
[c]*J. Heyrovský Institute of Physical Chemistry, v.v.i., Academy of Sciences of the Czech Republic, Dolejskova 3, CZ-18223 Prague, Czech Republic*

†Electronic supplementary information (ESI) available: X-ray crystallographic file for [**1**]ClO_4 and [**2**]ClO_4 in CIF format, mass spectrometry (Fig. S1), NMR spectra (Fig. S2), DFT optimised structures (Fig. S3), bond parameters (Tables S1–S4), DFT data (Tables S5–S17). CCDC 1465137 and 1465138. For ESI and crystallographic data in CIF or other electronic format see DOI: 10.1039/c6dt03764j

Results and discussion

Synthesis, general characterisation and crystal structures

The mononuclear complexes $[Os^{II}(bpy)_2(9\text{-OP})]ClO_4$ ([**1**]ClO_4) and $[Os^{II}(pap)_2(9\text{-OP})]ClO_4$ ([**2**]ClO_4) (bpy = 2,2′-bipyridine, pap = 2-phenylazopyridine, 9-OP^- = 9-oxidophenalenone) have been obtained *via* the reactions of H(9-OP) (9-hydroxyphenalenone) with the respective metal precursors *cis*-$[Os(bpy)_2Cl_2]$ and *ctc*-$[Os(pap)_2Cl_2]$ (*ctc* = *cis*–*trans*–*cis* configurations of chlorides, pyridine and azo nitrogen atoms, respectively) in the presence of Et_3N in a 2 : 1 EtOH–H_2O solvent mixture under a dinitrogen atmosphere, followed by precipitation using a saturated aqueous $NaClO_4$ solution. The complexes were purified by column chromatography using a neutral alumina column (Experimental) and characterized by their microanalytical data, electrical conductivity, mass spectrometry (Fig. S1†), IR and ^1H NMR spectroscopy (Fig. S2,† and the Experimental section).

The identities of the complexes [**1**]ClO_4 and [**2**]ClO_4 have been authenticated by their single crystal X-ray structures (Fig. 1, 2 and Tables 1, 2). In contrast to [**1**]$ClO_4{\cdot}C_6H_6$, the pap containing complex [**2**]ClO_4 (in *ctc* configuration) is not isostructural with the ruthenium analogue which crystallises as dichloromethane solvated [**4**]$ClO_4{\cdot}CH_2Cl_2$.[2a,b] The oxygen donors of 9-OP^- form a six-membered chelate with the $\{Os^{II}(bpy)_2\}$ or $\{Os^{II}(pap)_2\}$ fragments in [**1**]ClO_4 or [**2**]ClO_4, respectively. The appreciably shorter average *trans* (172.59°) and *cis*-angles (9-OP: 88.83°, bpy, 78.96°, pap: 77.3°) around the Os centre in the complexes illustrate a distorted octahedral situation. The shorter Os^{II}–N(pap) bond distance (average: 1.997 Å) compared to the Os^{II}–N(bpy) distance (average:

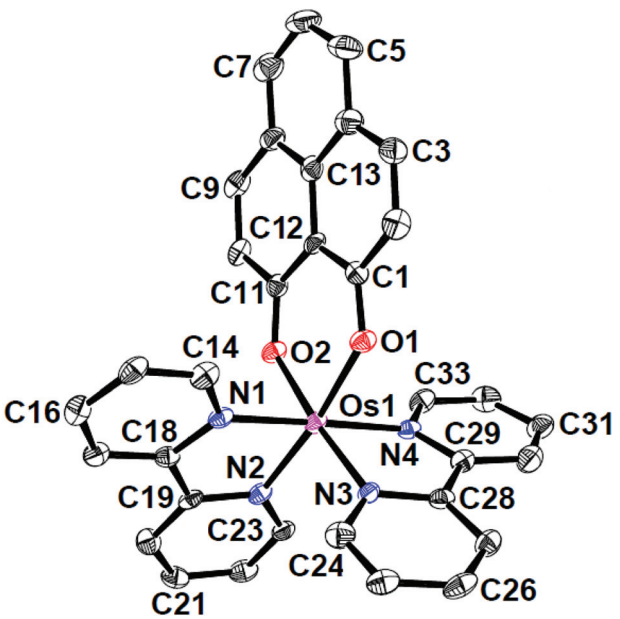

Fig. 1 ORTEP diagram of the cationic part of [**1**]$ClO_4{\cdot}C_6H_6$. Ellipsoids are drawn at the 50% probability level. Hydrogen atoms and solvent molecules are omitted for clarity.

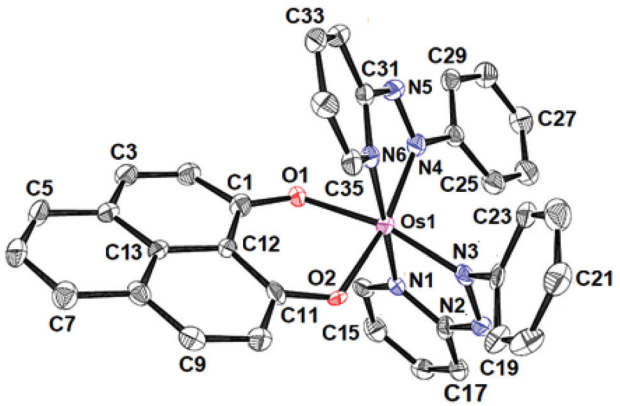

Fig. 2 ORTEP diagram of the cationic part of [**2**]ClO_4. Ellipsoids are drawn at the 50% probability level. Hydrogen atoms are omitted for clarity.

Table 1 Selected crystallographic data for [**1**]$ClO_4{\cdot}C_6H_6$ and [**2**]ClO_4

Complex	[**1**]$ClO_4{\cdot}C_6H_6$	[**2**]ClO_4
Empirical formula	$C_{39}H_{29}ClN_4O_6Os$	$C_{35}H_{25}ClN_6O_6Os$
Formula weight	875.35	851.26
Radiation	MoKα	MoKα
Crystal system	Triclinic	Monoclinic
Space group	$P\bar{1}$	$P2_1/c$
a/Å	11.694(3)	10.552(2)
b/Å	12.469(4)	19.785(3)
c/Å	13.505(4)	15.902(2)
α (°)	110.800(3)	90.00
β (°)	97.5790(10)	109.0190(10)
γ (°)	112.346(3)	90.00
V/Å^3	1619.5(8)	3138.6(9)
Z	2	4
μ/mm^{-1}	4.072	4.207
T/K	100(2)	100(2)
ρ_{calcd}/g cm^{-3}	1.795	1.801
F(000)	804	1672
θ range (°)	3.04 to 25.00	3.37 to 25.00
Data/restraints/parameters	5606/0/460	5441/0/442
R_1, wR_2 [$I > 2\sigma(I)$]	0.0290, 0.0651	0.0448,0.1035
R_1, wR_2 (all data)	0.0317, 0.0668	0.0528, 0.1115
GOF on F^2	1.047	0.991
Largest difference in peak and hole (e Å^{-3})	0.90/−0.68	2.68/−2.20

Table 2 Selected experimental and DFT calculated bond lengths (Å) for [**1**]$ClO_4{\cdot}C_6H_6$ and [**2**]ClO_4

	[**1**]$ClO_4{\cdot}C_6H_6$		[**2**]ClO_4	
Bond length (Å)	X-ray	DFT	X-ray	DFT
Os1–N1	2.037(3)	2.044	2.022(5)	2.031
Os1–N2	2.014(4)	2.017	—	—
Os1–N3	2.012(3)	2.017	1.956(6)	1.981
Os1–N4	2.048(3)	2.044	1.974(5)	1.976
Os1–N6	—	—	2.035(5)	2.046
Os1–O1	2.037(3)	2.037	2.030(4)	2.029
Os1–O2	2.042(3)	2.037	2.026(4)	2.032
C1–O1	1.297(5)	1.284	1.305(7)	1.286
C11–O2	1.292(5)	1.284	1.308(7)	1.288
N2–N3	—	—	1.335(7)	1.294
N4–N5	—	—	1.312(6)	1.288

2.028 Å)[8] reveals the stronger π-accepting feature of pap. Furthermore, the average Os^{II}–N(azo) distance is 0.06 Å shorter than the average Os^{II}–N(pyridine) distance of pap due to Os^{II} → azo(pap) back-bonding as has also been reflected in the lengthening of the N=N bond from 1.25 Å in free pap[9] to about 1.32 Å in [**2**]ClO_4. A remarkable amount of osmium(II)-to-pap π-back donation is evident from the rather short (<2.00 Å) metal-(azo)nitrogen distances and from the lengthened N–N bonds in the coordinated pap ligands in $\mathbf{2}^+$ (Table 2). Using a distance/oxidation state correlation for azo ligands[10a] one can imply a certain degree of contributions from pap radical anion ligands antiferromagnetically coupled with osmium(III). The σ and π electron donation from the $(9\text{-OP})^-$ ligand serves to enhance the electron density at the metal. The bond lengths within the $(9\text{-OP})^-$ ligand are in agreement with the standard description (including short C2C3 and C9C10 bonds, Scheme 1). Notably, the DFT calculations (Table 2) do not fully reproduce the experimental structural effects of the strong Os/pap π back donation (underestimation of N–N bond lengthening) which probably leads to the later discussed discrepancy of the spin distribution (Scheme 3).

The Os–N(bpy/pap) distance *trans* to the O donor of 9-OP^- is shorter than that of *trans* to N(bpy/pap) in [**1**]ClO_4/[**2**]ClO_4 due to the predominating σ-donating effect of the O donors. The average Os^{II}–O(9-OP) distances of 2.040 Å and 2.032 Å in [**1**]ClO_4 and [**2**]ClO_4 match fairly well with those of the reported analogous diketonate complexes of osmium(II).[10b] The average C–O bond distance in coordinated 9-OP of 1.29 Å in the complexes refers to its delocalized β-diketonate form.[11]

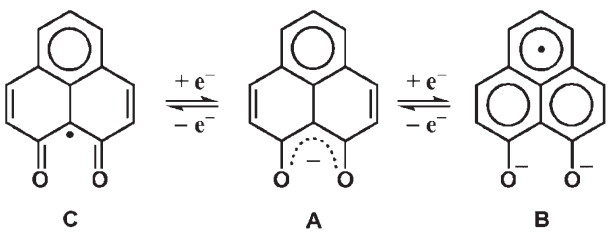

Scheme 1 Two-step redox series of $(9\text{-OP})^x$.

$$[Os^{III}(9\text{-}OP^-)(bpy)_2]^{2+} \longleftrightarrow [Os^{II}(9\text{-}OP^{\bullet})(bpy)_2]^{2+}$$

$$[Os^{III}(9\text{-}OP^-)(pap)_2]^{2+} \longleftrightarrow [Os^{II}(9\text{-}OP^{\bullet})(pap)_2]^{2+}$$

Scheme 3 Variable electronic structural situations in $\mathbf{1}^{2+}$ and $\mathbf{2}^{2+}$.

The experimental bond parameters of [**1**]ClO_4 and [**2**]ClO_4 (Table 2) are well reproduced by the DFT calculations (Table 2). These calculations also describe the bond length variations such as the shortening of Os–N bonds when going from [**1**]ClO_4 to [**2**]ClO_4. The bond length variations in the course of the redox processes are presented in Tables S1–S4, Fig. S3.†

Electrochemistry

The compounds [**1**]ClO_4 and [**2**]ClO_4 exhibit multiple oxidation (O1/O2) and reduction (R1–R3) processes within a potential window of ±2.0 V *versus* SCE in CH_3CN (Fig. 3, Table 3). The second oxidation wave (O2) is found to be irreversible in each case as is the third reduction of $\mathbf{1}^+$. An appreciable anodic shift of the redox potentials takes place on moving from the bpy containing [**1**]ClO_4 to [**2**]ClO_4 with the more π-accepting pap

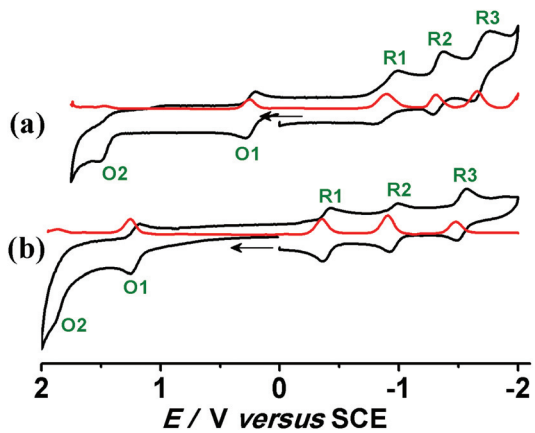

Fig. 3 Cyclic (black) and differential pulse (red) voltammograms in CH_3CN/0.1 M Et_4NClO_4 for (a) [**1**]ClO_4 and (b) [**2**]ClO_4 at 298 K.

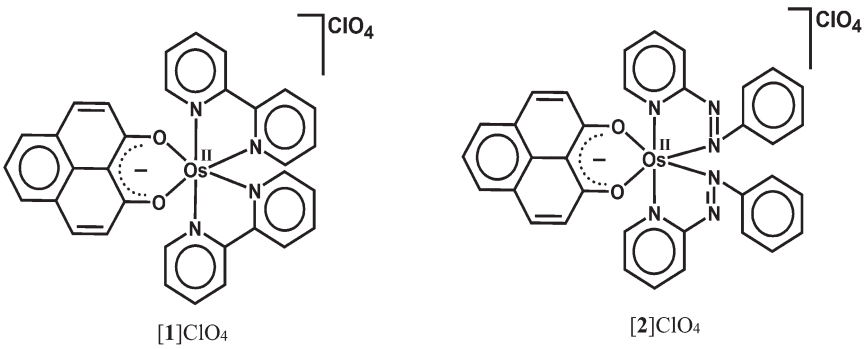

Scheme 2 Representation of complexes.

Table 3 Electrochemical data[a] at 298 K

	E°_{298}/V (ΔE_p/mV)[b]					K_c[c]				
Complex	O2[d]	O1	R1	R2	R3	K_{c1}[e]	K_{c2}[f]	K_{c3}[g]	K_{c4}[h]	Ref.
[**1**]ClO_4	1.49	0.24 (80)	−0.89 (150)	−1.32 (80)	−1.68 (110)	1.4×10^{21}	1.4×10^{19}	1.9×10^{7}	1.2×10^{6}	This work
[**2**]ClO_4	1.89	1.21 (60)	−0.39 (60)	−0.95 (60)	−1.52 (70)	3.3×10^{11}	1.3×10^{27}	3.1×10^{9}	4.5×10^{9}	This work
[**3**]ClO_4	1.78	0.50 (70)	−1.48 (70)	−1.74 (80)	—	4.9×10^{21}	3.6×10^{33}	2.5×10^{4}	—	2*a*
[**4**]ClO_4	—	1.22 (70)	−0.50 (60)	−1.00 (70)	—	—	1.4×10^{29}	2.9×10^{4}	—	2*b*

[a] From cyclic voltammetry in CH_3CN/0.1 M Et_4NClO_4 at 100 mV s^{-1}. [b] Potential in V *versus* SCE; peak potential differences ΔE_p/mV (in parentheses). [c] Comproportionation constant from $RT \ln K_c = nF(\Delta E)$. [d] Irreversible. [e] K_{c1} between O2 and O1. [f] K_{c2} between O1 and R1. [g] K_{c3} between R1 and R2. [h] K_{c4} between R2 and R3.

ligands. The effect of stronger π-donating Os^{II} in [**1**]ClO_4/[**2**]ClO_4 compared to Ru^{II} containing [**3**]ClO_4/[**4**]ClO_4 is similarly reflected by the change of the redox potentials (Table 3). The potentials for the first reversible oxidation decrease from the systems with π-accepting pap to the more electron rich bpy complexes, especially for the $\mathbf{1}^{+}/\mathbf{1}^{2+}$ transition with the π electron richer osmium. Conversely, the first reduction is the easiest for the pap complexes, especially for the $\mathbf{2}^{+}/\mathbf{2}$ transition, suggesting reduction of the acceptor ligands as will be shown later by EPR. The following reduction waves are more split in the case of $\mathbf{2}^{n}$, reflecting the stronger ligand–ligand interaction. The potential separations between successive redox processes of [**1**]ClO_4 and [**2**]ClO_4 are quantified by the comproportionation constants ($RT \ln K_c = nF(\Delta E)$).

The electronic structures of the redox states of $\mathbf{1}^{n}$ or $\mathbf{2}^{n}$ (3+, 2+, 1+, 0, 1−, 2−) have been ascertained by MO calculations (Tables S5–S17, Fig. S3†), EPR (Fig. 5, Tables 5 and S4†), Mulliken spin density distributions at the paramagnetic intermediate states (Table 4, Fig. 4), spectroelectrochemistry (Fig. 6) and TD-DFT calculations (Table 6).

Table 4 DFT calculated (UB3LYP/LanL2DZ/6-31G*) Mulliken spin densities for paramagnetic forms of $\mathbf{1}^{n}$ and $\mathbf{2}^{n}$

Complex	Os	bpy	pap	9-OP
$\mathbf{1}^{2+}$ ($S = 1/2$)	0.790	0.023	—	0.187
1 ($S = 1/2$)	0.000	0.844	—	0.188
$\mathbf{1}^{-}$ ($S = 1$)	−0.062	1.346	—	0.764
$\mathbf{1}^{2-}$ ($S = 3/2$)	0.372	1.674	—	1.028
$\mathbf{2}^{2+}$ ($S = 1/2$)	0.655	—	0.072	0.262
2 ($S = 1/2$)	−0.108	—	1.113	−0.003
$\mathbf{2}^{2-}$ ($S = 1/2$)	0.029	—	−0.008	1.032

EPR spectroscopy and spin density calculations

The odd-electron forms **1**/**2** and $\mathbf{1}^{2+}/\mathbf{2}^{2+}$ of the redox series $[Os(9\text{-OP})L_2]^{n}$ have been studied by *in situ* EPR spectroscopy. Electrolytic reduction of $\mathbf{1}^{+}$ at room temperature in CH_2Cl_2/0.1 M Bu_4NPF_6 produces an unresolved signal of **1** at $g_{iso} = 2.006$ (Fig. S4†), a typical value for complexes between the $bpy^{\bullet-}$ anion radical ligand[12] and diamagnetic metal complex

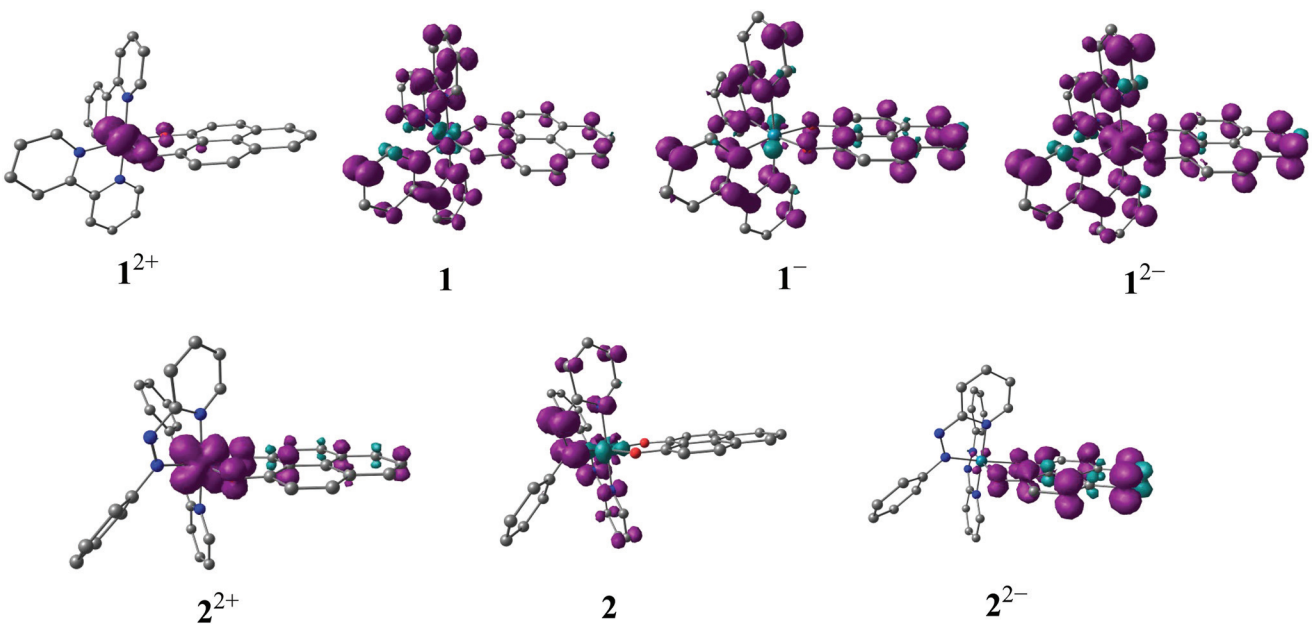

Fig. 4 DFT calculated Mulliken spin density plots for $\mathbf{1}^{n}$ and $\mathbf{2}^{n}$.

fragment.[13,14] An oxidation state description [Os^{II}(9-OP^{-})($bpy^{\bullet-}$)(bpy)] is thus formulated for **1**. At 120 K in frozen solution, a slight *g* factor anisotropy can be detected (Table 5, Fig. S4†) which is in agreement with a π type radical ion species.[12] A metal isotope coupling from ^{189}Os (16.1% nat. abundance, $I = 3/2$)[15] is detected at A_{iso} = 8 G (Fig. S4†) which confirms[8d] the calculated minor contribution from the metal to the spin distribution (Table 4, Fig. 4).

Oxidation to $\mathbf{1}^{2+}$ did not produce an EPR signal at ambient or low temperature, suggesting predominant spin location at the metal with its rather high spin–orbit coupling constant of about 3000 cm^{-1}.[15] Osmium(III) species are thus frequently EPR silent due to widely spread *g* components and rapid relaxation.[7] DFT spin density calculations confirm a bpy-based unpaired electron in **1** and an osmium(III) species $\mathbf{1}^{2+}$ (Table 4, Fig. 4).

Reduction of [Os^{II}(9-OP^{-})$(pap)_2$]$^{+}$ to **2** in the EPR cavity did not result in a detectable EPR signal at 298 or 120 K, although a pap-based unpaired electron is expected, as predicted also by DFT spin density calculations (Table 4, Fig. 4). As in previous studies[16] we assume facile electron hopping between equivalent (degenerate) sites for spin accommodation in [Os^{II}(9-OP^{-})($pap^{\bullet-}$)(pap)] which can result in severe EPR line broadening.[17] Apparently, the barrier for such intramolecular electron transfer [Os^{II}(9-OP^{-})($L^{\bullet-}$)(L°)] ⇌ [Os^{II}(9-OP^{-})(L°)($L^{\bullet-}$)] is very different in **1** and **2**. However, the expected pap based free radical EPR of **2** has been detected at 4 K which in effect corroborates the aforesaid rationale for its absence at higher temperature. Unexpectedly, the one-electron oxidation of $\mathbf{2}^{+}$ in CH_2Cl_2/0.1 M Bu_4NPF_6 gave an EPR signal at room temperature (g_{iso} = 1.986, Fig. S4†) which displayed a nearly axial *g* anisotropy in the frozen state at 125 K (Fig. 5, Table 5).

The signal detection even at 298 K, the isotropic *g* and the anisotropy $\Delta g = g_1 - g_3 = 0.061$ suggests[6,18] a predominantly ligand-based spin with minor metal contribution. The oxidizable ligand would be 9-OP^{-} which has been proven to exhibit a two-way non-innocent behaviour (9-$OP^{\bullet 2-}$/9-OP^{-}/9-$OP^{\bullet}$);[2a,b] the resulting species must then be formulated as [Os^{II}(9-$OP^{\bullet}$)$(pap)_2$]$^{2+}$. This experimental result is in full agreement with the notion[19] that strongly π-accepting pap stabilises the lower valent state (here Os^{II}) which in turn leaves only the ligand remaining for oxidation (Scheme 3). Similar strategies have been employed for ruthenium complexes of triazenides or amidines which are oxidised to triazenyl or amidinyl complexes when the metal is made electron-poor through the coordination of π acceptors.[4c,20]

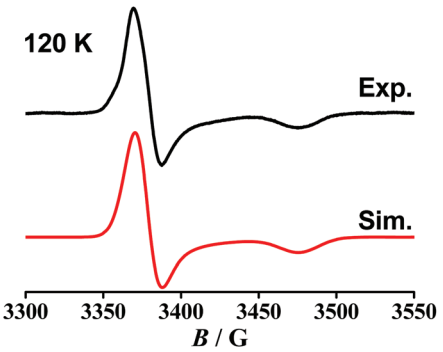

Fig. 5 EPR spectrum of $\mathbf{2}^{2+}$ after *in situ* oxidation of [**2**]ClO_4 in CH_2Cl_2/0.1 M Bu_4NPF_6.

The bpy containing system $\mathbf{1}^{n}$ is obviously more susceptible to metal-based oxidation in $\mathbf{1}^{2+}$ due to the less pronounced π-acceptor strength of the 2,2′-bipyridine co-ligands (Scheme 3).

The experimental results illustrated in Scheme 3 could not be satisfactorily reproduced by DFT calculations. For instance, a metal centred spin was calculated for both $\mathbf{1}^{2+}$ and $\mathbf{2}^{2+}$. However, the *g* parameters and Os hyperfine coupling constant for neutral **1** were reasonably reproduced by DFT. Attempts to obtain the optimised structure corresponding to the state with a spin localised at the ligand in $\mathbf{2}^{2+}$ were unsuccessful. This discrepancy may be caused by the existence of two closely lying minima with a low energy barrier and by the failure of one-determinant DFT to fully reproduce the pronounced structural effects of strong osmium-to-pap π back donation in order to reach the appropriate minimum.

The ambivalent situation as illustrated in Scheme 3, *i.e.* the generation of an intramolecular oxidation state shift through the variation of the ancillary ligands can be similarly observed *e.g.* for copper/quinone[21] and iron/quinone compounds[22] (Scheme 4) where such redox isomer alternatives can have biochemical implications.[23]

For a heavy $5d^{n}$ transition metal from the platinum metal group, this kind of redox isomerism is reported here for the first time.

Other oxidation states accessible by spectroelectrochemistry were EPR silent. The precursor complexes $\mathbf{1}^{+}$ and $\mathbf{2}^{+}$ are $S = 0$ species as is the spin ground state of $\mathbf{2}^{-}$ (Scheme 5) while $\mathbf{1}^{-}$ is a triplet species (Scheme 5). For $\mathbf{2}^{2-}$ the DFT calculations suggest an $S = 1/2$ spin ground state with two antiferromagnetically coupled $pap^{\bullet-}$ ligands whereas $\mathbf{1}^{2-}$ was calculated to

Table 5 EPR data of paramagnetic intermediates[a]

Complex	g_{iso} (298 K)	g_1 (120 K)	g_2	g_3	$\langle g \rangle$[c]	Δg[d]
1 (Exp.)	2.006[b]	2.022	2.005	1.986	2.004	0.036
1 (Calc.)	1.991	2.008	2.003	1.964	1.991	0.044
2	n.o.	1.98 (4 K)	1.94	1.89	1.937	0.09
$\mathbf{2}^{2+}$	1.986	2.007	2.004	1.946	1.985	0.061

[a] From *in situ* electrolysis in CH_2Cl_2/0.1 M Bu_4NPF_6. [b] $\alpha_{iso}(^{189}Os)$ = 8.0 G, calculated $\alpha_{iso}(^{189}Os)$ = 7.7 G. [c] $\langle g \rangle = \{(1/3)(g_1^2 + g_2^2 + g_3^2)\}^{1/2}$. [d] $\Delta g = g_1 - g_3$.

$$M^{n+} / Q^{2-} \quad \textit{versus} \quad M^{n-1} / Q^{\bullet-}$$

$$Q = \text{quinone}, M^{n+} = Fe^{3+} \text{ or } Cu^{2+}$$

Scheme 4 Metal/quinone oxidation state ambivalence.

$\mathbf{1}^{2+}/\mathbf{2}^{2+}$: $[Os^{III}(9\text{-}OP^{-})L_2]^{2+}$ (L = bpy : S = 1/2)
or
$[Os^{II}(9\text{-}OP^{\bullet})L_2]^{2+}$ (L = pap : S = 1/2)

$-e^{-}$ ⇅ $+e^{-}$

$\mathbf{1}^{+}/\mathbf{2}^{+}$: $[Os^{II}(9\text{-}OP^{-})L_2]^{+}$ (S = 0)

$-e^{-}$ ⇅ $+e^{-}$

1/ 2 : $[Os^{II}(9\text{-}OP^{-})(L^{\bullet-})L]^{0}$ (S = 1/2)

$-e^{-}$ ⇅ $+e^{-}$

$\mathbf{1}^{-}/\mathbf{2}^{-}$: $[Os^{II}(9\text{-}OP^{\bullet 2-})(L^{\bullet-})L]^{-}$ (L = bpy : S=1)
or
$[Os^{II}(9\text{-}OP^{-})(L^{\bullet-})_2]^{-}$ (L = pap : S = 0)[a]

$-e^{-}$ ⇅ $+e^{-}$

$\mathbf{1}^{2-}/\mathbf{2}^{2-}$: $[Os^{II}(9\text{-}OP^{\bullet 2-})(L^{\bullet-})_2]^{2-}$ (L = bpy: S=3/2, or L = pap: S = 1/2)[b]

[a] $\Delta E_{S=1\text{-}S=0} = 289\ cm^{-1}$

[b] $\Delta E_{(S=1/2)\text{-}(S=3/2)} = 2146\ cm^{-1}$ ($\mathbf{1}^{2-}$) and $\Delta E_{(S=3/2)-(S=1/2)} = 1964\ cm^{-1}$ ($\mathbf{2}^{2-}$)

Scheme 5 Assignments of most appropriate oxidation states within the redox series $\mathbf{1}^{n}$ and $\mathbf{2}^{n}$.

have an S = 3/2 ground state; however, this latter form could not be generated reversibly. The DFT calculated structures and MO compositions (Tables S5–S17†) confirm the following assignments.

UV-vis-NIR spectroelectrochemistry and TD-DFT calculations

According to UV-vis-NIR spectroelectrochemistry, using an optically transparent thin-layer electrolysis (OTTLE) cell,[24] reversible electron transfer processes could be monitored for transitions $\mathbf{1}^{2+}$–$\mathbf{1}^{-}$ and $\mathbf{2}^{2+}$–$\mathbf{2}^{2-}$. This approach allowed us to study the EPR active and EPR silent species as well as diamagnetic states. The spectra are shown in Fig. 6 while the absorption data are summarised in Table 6 together with the results from time-dependent DFT (TD-DFT) calculations.

The structurally characterised precursor cations $[Os^{II}(9\text{-}OP^{-})L_2]^{+}$ exhibit the expected metal-to-ligand charge transfer (MLCT) transitions in the visible, with the π* orbitals of the acceptors bpy or pap as the target. Compared with the ruthenium analogues $\mathbf{3}^{+}$ and $\mathbf{4}^{+}$ (ref. 2*a*,*b*) the osmium compounds exhibit decreased MLCT transition energy, in agreement with the more destabilised metal d orbitals of the heavier homologue. Ligand-to-ligand charge transfer (LLCT) and intra-ligand (IL) transitions occur at higher energies than the MLCT absorptions (Table 6).

The ligand (L)-based reduction of the compounds results in shifted MLCT bands and in typically[25] weak "intra-radical" bands in the near infrared regions.[26] While the spectral response is similar for **1** and **2**, the two-electron reduced forms $\mathbf{1}^{-}$ and $\mathbf{2}^{-}$ differ considerably, both spectroscopically and according to the TD-DFT calculation results. Whereas spin–spin coupling between the two $pap^{\bullet-}$ ligands leads to a diamagnetic species $\mathbf{2}^{-}$ (S = 0) with only one major band in the visible region (metal-to-(9-OP) ligand charge transfer), the corresponding system $\mathbf{1}^{-}$ with two $bpy^{\bullet-}$ ligands is computed with an S = 1 spin ground state and various LLCT and MLCT transitions in the near infrared and visible regions (Fig. 6, Table 6). The $\mathbf{2}^{-}$ form, reversibly accessible only for the pap-containing series, exhibits several absorptions in the visible, mostly of MLCT character.

The oxidised forms $\mathbf{1}^{2+}$ and $\mathbf{2}^{2+}$ were identified as rather different (Scheme 5) through EPR spectroscopy, although the DFT calculations did not well reproduce the experimentally observed (9-OP) ligand-centred spin distribution. Therefore, the TD-DFT results must also be used with caution although the absorption spectral data appear generally well reproduced (Table 6). However, a look at the spectra (Fig. 6) illustrates a rather different appearance of $\mathbf{1}^{2+}$ and $\mathbf{2}^{2+}$ in the visible region, which suggests qualitatively different electronic structures as deduced already from the EPR studies (Scheme 5).

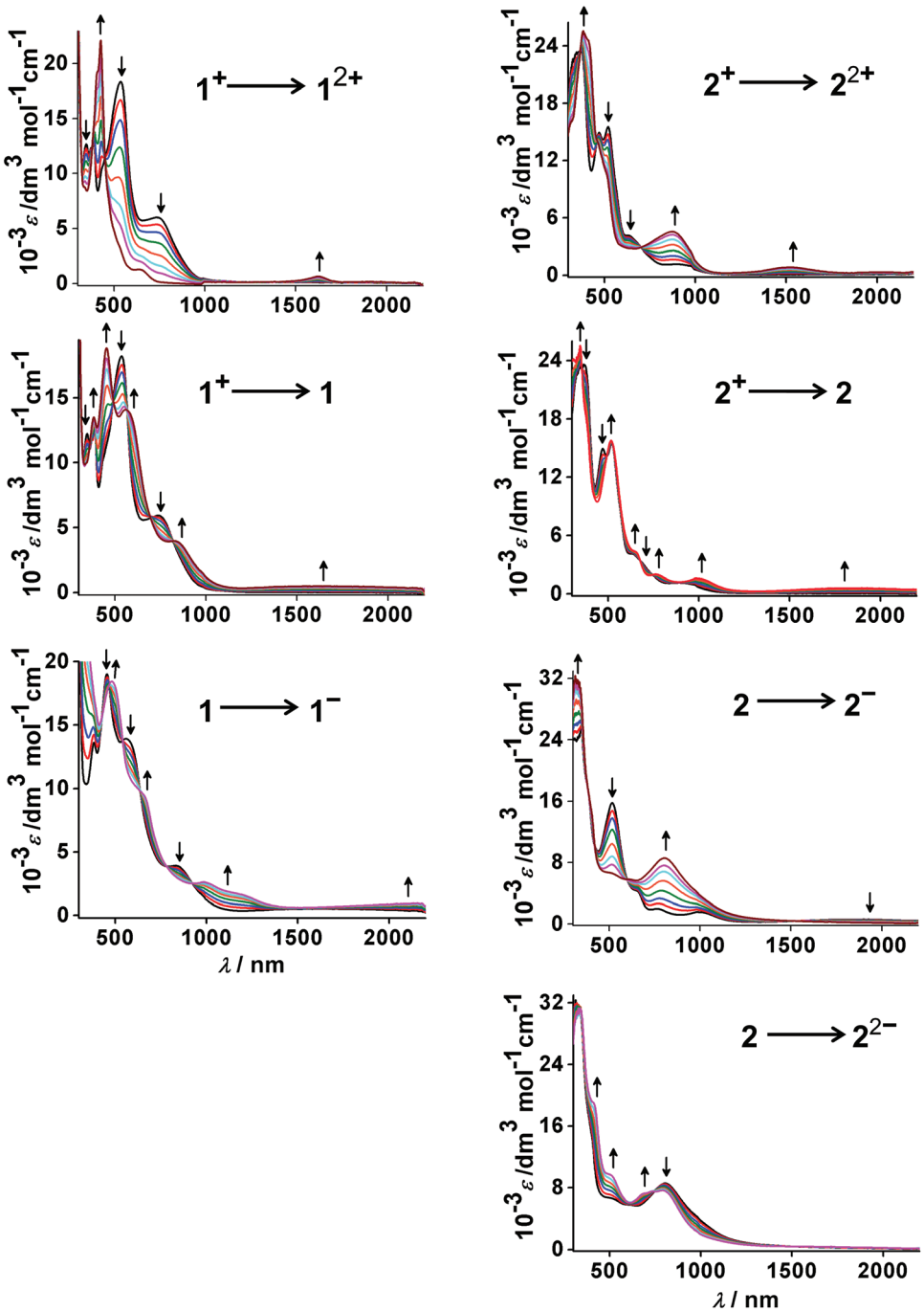

Fig. 6 UV-vis-NIR spectroelectrochemistry of $\mathbf{1}^n$ and $\mathbf{2}^n$ (n = 2+, 1+, 0, 1–, 2–) in CH_3CN/0.1 M Bu_4NPF_6.

Conclusion

The present study is complementary to previous reports[2,5] on iron and ruthenium complexes with a non-innocent 9-oxidophenalenone ligand. The use of the heavier group 8 metal osmium produces a remarkable array of differences for all four members of the redox series $[Os(9\text{-}OP)L_2]^n$, n = 2+, +, 0, −, when the co-ligands L are changed from bpy to the more π-accepting pap.

The combination between the third-row transition metal osmium and two different kinds of non-innocently behaving ligands in complexes $[Os(9\text{-}OP)L_2]^n$ (L = bpy or pap) produced a redox series with remarkably diverse oxidation state arrangements.

(i) Even the structurally characterised precursor cations $[Os^{II}(9\text{-}OP^{-})L_2]^+$ exhibit a notable difference between the more conventional $\mathbf{1}^+$ and the pap-containing ion $\mathbf{2}^+$ with significant structural effects of very strong d(Os) → π*(pap) back donation.

(ii) Starting from there, the spectroelectrochemical studies and partially successful calculations revealed the expected reduction of one of the acceptor ligands L. However, the

Table 6 Experimental and TD-DFT ((U)B3LYP/CPCM/CH_3CN) calculated electronic transitions for $\mathbf{1}^n$ and $\mathbf{2}^n$

$\lambda_{max}{}^{a,b}$ ($\lambda_{TDDFT}{}^{b}$)	(ε/dm^3 mol^{-1} cm^1)^{a,c} (f)^d	Transitions	Character
$\mathbf{1}^{2+}$ (S = 1/2)			
1622 (2100)	650 (0.002)	HOMO−1(β) → LUMO(β)(90)	9-OP(π) → Os(dπ)
635 (652)	1290 (0.026)	HOMO−2(β) → LUMO(β)(73)	Os(dπ) → Os(dπ)
426 (434)	22 130 (0.066)	HOMO(α) → LUMO+3(α)(78)	9-OP(π) → 9-OP(π*)
410 (408)	820 (0.047)	HOMO−1(α) → LUMO+1(α)(86)	9-OP(π) → bpy(π*)
288 (287)	28 670 (0.017)	HOMO−1(α) → LUMO+6(α)(51)	9-OP(π) → bpy(π*)
242 (256)	29 590 (0.031)	HOMO−3(α) → LUMO+3(α)(86)	9-OP(π)/bpy(π) → bpy(π*)
$\mathbf{1}^{+}$ (S = 0)			
739 (625)	5920 (0.012)	HOMO → LUMO(52)	Os(dπ) → bpy(π*)
537 (557)	18 230 (0.023)	HOMO−1 → LUMO+1(54)	Os(dπ) → bpy(π*)
391 (361)	12 720 (0.051)	HOMO−3 → LUMO(67)	9-OP(π) → bpy(π*)
347 (342)	12 240 (0.095)	HOMO−3 → LUMO+2(64)	9-OP(π) → 9-OP(π*)
294 (296)	41 790 (0.024)	HOMO−5 → LUMO(66)	9-OP(π) → bpy(π*)
241 (239)	29 210 (0.061)	HOMO−5 → LUMO+3(60)	9-OP(π) → bpy(π*)
$\mathbf{1}$ (S = 1/2)			
1650 (1057)	480 (0.0013)	HOMO(α) → LUMO+2(α)(98)	9-OP(π) → 9-OP(π*)
825 (869)	3950 (0.004)	HOMO−1(α) → LUMO+1(α)(51)	Os(dπ) → 9-OP(π*)
557 (552)	14 070 (0.048)	HOMO−2(β) → LUMO+1(β)(59)	Os(dπ) → bpy(π*)
454 (444)	18 840 (0.144)	HOMO−2(β) → LUMO+2(β)(64)	Os(dπ) → bpy(π*)
384 (380)	13 520 (0.019)	HOMO−3(β) → LUMO+1(β)(63)	9-OP(π) → bpy(π*)
296 (295)	33 940 (0.004)	HOMO−5(β) → LUMO+1(β)(64)	bpy(π) → bpy(π*)
243 (255)	29 700 (0.014)	HOMO−5(β) → LUMO+4(β)(64)	9-OP(π) → bpy(π*)
$\mathbf{1}^{-}$ (S = 1)			
2200 (2519)	950 (0.037)	HOMO−1(α) → LUMO(α)(71)	9-OP(π)/bpy(π) → bpy(π*)
1150 (992)	590 (0.001)	HOMO−1(α) → LUMO+1(α)(74)	9-OP(π)/bpy(π) → bpy(π*)
986 (934)	2630 (0.014)	HOMO−1(α) → LUMO(α)(85)	Os(dπ) → bpy(π*)/9-OP(π*)
635 (650)	8330 (0.004)	HOMO−1(β) → LUMO+1(β)(55)	Os(dπ) → bpy(π*)
480 (470)	18 440 (0.002)	HOMO−2(α) → LUMO+1(α)(71)	Os(dπ) → bpy(π*)
306 (303)	26 950 (0.040)	HOMO−5(β) → LUMO(β)(60)	bpy(π) → 9-OP(π*)
$\mathbf{2}^{2+}$ (S = 1/2)			
1515 (1961)	830 (0.004)	HOMO−1(β) → LUMO(β)(83)	9-OP(π) → Os(dπ)
872 (839)	4540 (0.035)	HOMO−3(β) → LUMO(β)(50)	pap(π)/Os(dπ) → Os(dπ)/9-OP(π*)
512 (526)	10 670 (0.002)	HOMO−9(β) → LUMO(β)(76)	pap(π)/9-OP(π) → Os(dπ)/9-OP(π*)
383 (383)	25 580 (0.045)	HOMO−2(β) → LUMO+2(β)(57)	pap(π) → 9-OP(π*)
$\mathbf{2}^{+}$ (S = 0)			
896 (699)	1130 (0.006)	HOMO−1 → LUMO(65)	Os(dπ)/9-OP(π) → pap(π*)
635 (637)	4120 (0.008)	HOMO → LUMO+1(59)	9-OP(π)/Os(dπ) → pap(π*)
520 (590)	15 500 (0.011)	HOMO−1 → LUMO+1(62)	Os(dπ)/9-OP(π) → pap(π*)/9-OP(π*)
469 (471)	14 950 (0.012)	HOMO → LUMO+2(69)	9-OP(π)/Os(dπ) → 9-OP(π*)
367 (354)	23 620 (0.039)	HOMO−3 → LUMO+2(65)	pap(π)/9-OP(π) → 9-OP(π*)
343 (322)	23 240 (0.074)	HOMO−4 → LUMO+2(69)	pap(π) → 9-OP(π*)
$\mathbf{2}$ (S = 1/2)			
1880 (1650)	580 (0.019)	HOMO(α) → LUMO+1(α)(95)	pap(π) → pap(π*)/Os(dπ)
996 (1078)	1560 (0.001)	HOMO(α) → LUMO(α)(95)	pap(π) → P(π*)
762 (722)	1990 (0.014)	HOMO(β) → LUMO(β)(77)	Os(dπ)/pap(π) → 9-OP(π*)
642 (603)	4040 (0.001)	HOMO−2(α) → LUMO(α)(58)	Os(dπ)/9-OP(π) → 9-OP(π*)
517 (513)	15 780 (0.047)	HOMO−1(β) → LUMO+1(β)(79)	Os(dπ)/pap(π) → pap(π*)
346 (348)	25 460 (0.014)	HOMO−4(β) → LUMO+1(β)(86)	9-OP(π)/pap(π) → pap(π*)
308 (302)	23 990 (0.018)	HOMO−7(β) → LUMO+2(β)(81)	pap(π) → pap(π*)
$\mathbf{2}^{-}$ (S = 0)			
804 (637)	8570 (0.032)	HOMO−2 → LUMO(66)	Os(dπ)/pap(π) → 9-OP(π*)
320 (331)	31 850 (0.044)	HOMO−5 → LUMO+1(51)	pap(π) → pap(π*)
$\mathbf{2}^{2-}$ (S = 1/2)			
790 (850)	7650 (0.008)	HOMO(β) → LUMO+1(β)(98)	pap(π)/Os(dπ) → 9-OP(π*)
738 (706)	7530 (0.005)	HOMO−3(α) → LUMO(α)(55)	Os(dπ)/pap(π) → pap(π*)
690 (632)	7250 (0.020)	HOMO−4(α) → LUMO(α)(65)	Os(dπ)/pap(π) → pap(π*)
519 (538)	9520 (0.027)	HOMO−2(β) → LUMO+1(β)(71)	Os(dπ)/pap(π) → 9-OP(π*)
415 (415)	18 970 (0.007)	HOMO(α) → LUMO+7(α)(64)	9-OP(π) → 9-OP(π*)
335 (361)	31 090 (0.038)	HOMO−5(β) → LUMO+1(β) (61)	9-OP(π) → 9-OP(π*)

[a] Experimental absorption maxima (λ_{max} > 300 nm) from OTTLE spectroelectrochemistry in CH_3CN/0.1 M Bu_4NPF_6. [b] In nm. [c] Molar extinction coefficients in dm^3 mol^{-1} cm^1. [d] Calculated oscillator strengths.

absence of an EPR signal for $[Os^{II}(9\text{-}OP^{-})(pap^{\bullet-})(pap)]^0$ in contrast to $[Os^{II}(9\text{-}OP^{-})(bpy^{\bullet-})(bpy)]^0$ (and $[Ru^{II}(9\text{-}OP^{-})L_2]^0$)^{2a,b} points to different dynamics (barrier) for intramolecular electron exchange ("spin hopping") between $L^{\bullet-}$ and L.

(iii) Furthermore surprising is the dichotomous behaviour on oxidation of the precursors to $[Os(9\text{-}OP)L_2]^{2+}$: whereas the EPR silence of the bpy containing a complex ion suggests a metal-oxidised form $[Os^{III}(9\text{-}OP^{-})(bpy)_2]^{2+}$, similar to both

ruthenium species $[Ru^{III}(9\text{-}OP^{-})L_2]^{2+}$ (L = bpy[2a] and pap[2b]), the stabilisation of the divalent metal state through strong π*(pap) to d(Os) back donation leads to an EPR-spectroscopically evidenced oxidation of the β-diketonate ligand 9-oxidophenalenone to the corresponding neutral radical ligand (Schemes 3 and 5).

This unexpected ambivalence, the first recognized here for a $5d^n$ transition metal situation, represents another case of "hidden" noninnocence[4b] and may be related to similar observations in the biochemically relevant metal/quinone series (Fe, Cu; Scheme 4). Computational approaches to such ambivalent arrangements are difficult[27] as confirmed here, and more sophisticated methods will have to be applied.

(iv) Although not accessible by EPR but supported by spectroelectrochemistry there is a further dichotomy suggested by DFT calculations for the two-electron reduction products $[Os^{II}(9\text{-}OP^{-})(L^{\bullet-})_2]^{-}$, with antiferromagnetically coupled $pap^{\bullet-}$ ligands ($S = 0$) in contrast to the case with $L^{\bullet-}$ = bpy ($S = 1$).

Summarising, in the series of Ru/Os and bpy/pap combinations $\mathbf{1}^n$–$\mathbf{4}^n$ the osmium(II)-pap π backbonding is clearly distinguished by its strength, causing structural effects, dichotomous metal–ligand spin shifts, and strong inter-ligand interactions resulting in spin isomerism and variable electron hopping.

Experimental section

Materials

The starting metal precursors, *cis*-$[Os(bpy)_2Cl_2]$[28] and *ctc*-$[Os(pap)_2Cl_2]$[29] and the ligand precursor, 9-hydroxy-1*H*-phenalen-1-one (H(9-OP)),[30] were prepared according to the reported procedures. Other chemicals and solvents were of reagent grade and used as received. For spectroscopic and electrochemical studies, HPLC grade solvents were used.

Physical measurements

The electrical conductivity of solutions was checked by using an autoranging conductivity meter (Toshcon Industries, India). ^{1}H NMR spectra were recorded on a Bruker Avance III 500 MHz spectrometer. The EPR measurements were made in a two electrode capillary tube[31] with an X-band (9.5 GHz) Bruker system ESP300 spectrometer; for better formation of glassy frozen solutions the measurements were performed in CH_2Cl_2/0.1 M Bu_4NPF_6. Cyclic voltammetric and differential pulse voltammetric measurements of the complexes were done using a PAR model 273A electrochemistry system under a dinitrogen atmosphere. A glassy carbon-working electrode, a platinum wire auxiliary electrode, and a saturated calomel reference electrode (SCE) were used in a standard three-electrode configuration with tetraethylammonium perchlorate (TEAP) as the supporting electrolyte and a scan rate of 100 mV s^{-1}. UV-vis-NIR spectroelectrochemical experiments were performed in CH_3CN/0.1 M Bu_4NPF_6 at 298 K using an optically transparent thin-layer electrode cell (OTTLE) mounted in the sample compartment of a J&M TIDAS spectrophotometer.[24] All spectroelectrochemical experiments were performed under a dinitrogen atmosphere. Elemental analyses were performed on a Perkin Elmer 240C elemental analyser. IR spectra of the complexes as KBr pellets were recorded on a Nicolet spectrophotometer. Electrospray mass spectra (ESI-MS) were recorded on a Bruker Maxis Impact instrument (282 001.00081). Program easyspin-4.5.5 with Matlab R2014b was used for EPR simulation.[32]

Preparation of complexes

Synthesis of $[Os^{II}(bpy)_2(9\text{-}OP)]ClO_4$, $[\mathbf{1}]ClO_4$. A mixture of *cis*-$[Os(bpy)_2Cl_2]$ (100 mg, 0.17 mmol), H(9-OP) (37 mg, 0.19 mmol) and NEt_3 (20 mg, 0.2 mmol, freshly distilled over KOH) was taken in 40 cm^3 of 2 : 1 ethanol : water and refluxed under a dinitrogen atmosphere for 72 h. The initial light brown colour of the solution gradually changed to dark violet. The reaction mixture was evaporated to dryness, the crude product was redissolved in a minimum volume of CH_3CN, and 10 cm^3 saturated $NaClO_4$ solution was added. The resulting violet precipitate was filtered off and washed twice with ice-cold distilled water and dried under vacuum. The crude product was purified by using a neutral alumina column. The pure violet complex $[\mathbf{1}]ClO_4$ was eluted by a 5 : 1 solvent mixture of dichloromethane–acetonitrile. Evaporation of the solvent under reduced pressure yielded pure $[\mathbf{1}]ClO_4$.

$[\mathbf{1}]ClO_4$: yield: 75 mg, 61%. Anal. calcd for $C_{33}H_{23}ClN_4O_6Os$: C, 49.72; H, 2.91; N, 7.03; found: C, 50.01; H, 3.02; N, 6.98. Λ_M (Ω^{-1} cm^2 M^{-1}) in acetonitrile at 298 K: 95. ESI-MS(+) in CH_3CN, *m*/*z* calcd for $\{\mathbf{1}^+\}$: 697.79; found: 697.13. ^{1}H-NMR (400 MHz, $CDCl_3$): δ(ppm, *J*(Hz)): 8.46 (d, 2H, 8.04), 8.34 (d, 1H, 8.0), 8.22 (d, 2H, 7.7), 8.16 (d, 2H, 7.5), 8.06 (d, 2H, 9.3), 7.65 (t, 2H, 7.7), 7.36–7.45 (m, 6H), 7.17 (d, 2H, 7.4), 6.93 (t, 2H, 6.7), 6.88 (d, 2H, 8.2). ν(ClO_4^-, cm^{-1}): 1090, 622.

Synthesis of $[Os^{II}(pap)_2(L)]$, $[\mathbf{2}]ClO_4$. A mixture of *ctc*-$[Os(pap)_2Cl_2]$ (100 mg, 0.16 mmol), H(9-OP) (34 mg, 0.17 mmol) and NEt_3 (20 mg, 0.2 mmol, freshly distilled over KOH) in 40 cm^3 of 2 : 1 ethanol : water was refluxed under a dinitrogen atmosphere for 72 h. The initial violet colour of the solution gradually turned to dark red. The reaction mixture was evaporated to dryness. It was redissolved in a minimum volume of CH_3CN and a saturated solution of $NaClO_4$ (10 cm^3) was added. The resulting red precipitate was filtered off, washed twice with ice-cold distilled water and dried under vacuum. It was purified further by using a neutral alumina column. The pure red complex $[\mathbf{2}]ClO_4$ was eluted by a 8 : 1 dichloromethane–acetonitrile solvent mixture. Evaporation of the solvent under reduced pressure yielded pure $[\mathbf{2}]ClO_4$.

$[\mathbf{2}]ClO_4$: yield: 80 mg, 67%. Anal. calcd for $C_{35}H_{25}ClN_6O_6Os$: C, 49.38; H 2.96; N 9.87; found: C, 49.51; H, 3.05; N, 9.89. Λ_M (Ω^{-1} cm^2 M^{-1}) in acetonitrile at 298 K: 106. ESI-MS(+) in CH_3CN, *m*/*z* calcd for $\{\mathbf{2}^+\}$: 751.84; found: 751.17. ^{1}H-NMR (400 MHz, $CDCl_3$): δ(ppm, *J*(Hz)):8.69 (d, 2H, 8.2), 8.05 (m, 4H), 7.89 (t, 2H, 7.7), 7.64–7.68 (m, 3H), 7.34 (t, 2H, 7.5), 7.15–7.28 (m, 8H), 6.71 (d, 4H, 8.1). ν(ClO_4^-, cm^{-1}): 1093, 619.

(**Caution**! Perchlorate salts are explosive and should be handled with care).

Crystal structure determination

Single crystals of [**1**]ClO_4 and [**2**]ClO_4 were grown by slow evaporation of 1 : 1 CH_2Cl_2–benzene and 1 : 2 CH_3CN–benzene solutions, respectively. X-ray crystal data were collected on a RIGAKU SATURN-724+ CCD single crystal X-ray diffractometer using Mo-Kα radiation. Data collection was evaluated by using the CrystalClear-SM Expert software. The data were collected by the standard ω-scan technique. The structure was solved by direct methods using SHELXS-97 and refined by full matrix least squares with SHELXL-97, refining on F^2.[33] All non-hydrogen atoms were refined anisotropically. The hydrogen atoms were placed in geometrically constrained positions and refined with isotropic temperature factors, generally $1.2U_{eq}$ of their parent atoms. Hydrogen atoms were included in the refinement process as per the riding model. CCDC no. 1465137 and 1465138 contain the supplementary crystallographic data for [**1**]ClO_4 and [**2**]ClO_4, respectively.

Computational details

Calculations were performed with Gaussian09[34] and ADF 2016.01[35] program packages. DFT geometry optimization of $\mathbf{1}^+$ and $\mathbf{2}^+$ utilized the Perdew, Burke, Ernzerhof hybrid functional[36] (PBE0) together with quasi-relativistic effective core pseudopotentials and a correspondingly optimised set of basis functions for Os[37] and the polarized triple ζ basis set 6-311 g (d)[38] for the remaining atoms. In order to rationalise the computation time, geometry optimisations within the whole series were carried out by using the density functional theory method at the (R)B3LYP level for $\mathbf{1}^+$, $\mathbf{2}^+$, $\mathbf{2}^-$ and the (U)B3LYP level[39] for $\mathbf{1}^{3+}$, $\mathbf{1}^{2+}$, **1**, $\mathbf{1}^-$, $\mathbf{1}^{2-}$ and $\mathbf{2}^{3+}$, $\mathbf{2}^{2+}$, **2**, $\mathbf{2}^{2-}$ with the Gaussian 09 program package.[34] Except osmium all other elements were assigned the 6-31G* basis set. The LANL2DZ basis set with an effective core potential was employed for the osmium atom.[37] The vibrational frequency calculations were performed to ensure that the optimised geometries represent the local minima and there are only positive eigenvalues. Vertical electronic excitations based on (R)B3LYP/(U)B3LYP optimized geometries were computed for $\mathbf{1}^n$ (n = +2, +1, 0, −1) and $\mathbf{2}^n$ (n = +2, +1, 0, −1, −2) using the time-dependent density functional theory (TD-DFT) formalism[40] in acetonitrile using the conductor-like polarisable continuum model (CPCM).[41] *A* and *g* tensors were obtained by first-order perturbation theory from a ZORA Hamiltonian[42,43] in the presence of a time-independent magnetic field.[44] The *g* tensor was obtained from a spin-non-polarised wave function after incorporating the spin–orbit (SO) coupling using the PBE0 functional. *Chemissian* 1.7[45] was used to calculate the fractional contributions of various groups to each molecular orbital. All calculated structures were visualised with *ChemCraft*.[46]

Acknowledgements

Financial support received from the Department of Science and Technology, University Grant Commission (fellowship to A. H.), New Delhi (India) and the Land Baden-Württemberg (Germany) is gratefully acknowledged.

References

1 (*a*) S. K. Mandal, S. Samanta, M. E. Itkis, D. W. Jensen, R. W. Reed, R. T. Oakley, F. S. Tham, B. Donnadieu and R. C. Haddon, *J. Am. Chem. Soc.*, 2006, **128**, 1982–1994; (*b*) S. K. Pal, F. S. Tham, R. W. Reed, R. T. Oakley and R. C. Haddon, *Polyhedron*, 2005, **24**, 2076–2083; (*c*) T. K. Sen, A. Mukherjee, A. Modak, P. K. Ghorai, D. Kratzert, M. Granitzka, D. Stalke and S. K. Mandal, *Chem. –Eur. J.*, 2012, **18**, 54–58.

2 (*a*) A. Das, T. Scherer, S. M. Mobin, W. Kaim and G. K. Lahiri, *Inorg. Chem.*, 2012, **51**, 4390–4397; (*b*) A. Das, T. Scherer, P. Mondal, S. M. Mobin, W. Kaim and G. K. Lahiri, *Chem. – Eur. J.*, 2012, **18**, 14434–14443; (*c*) H. Agarwala, T. Scherer, S. M. Mobin, W. Kaim and G. K. Lahiri, *Dalton Trans.*, 2014, **43**, 3939–3948; (*d*) A. Das, T. K. Ghosh, A. D. Chowdhury, S. M. Mobin and G. K. Lahiri, *Polyhedron*, 2013, **52**, 1130–1137.

3 W. Kaim, *Inorg. Chem.*, 2011, **50**, 9752–9765.

4 (*a*) A. Mandal, A. Grupp, B. Schwederski, W. Kaim and G. K. Lahiri, *Inorg. Chem.*, 2015, **54**, 7936–7944; (*b*) M. M. Khusniyarov, E. Bill, T. Weyhermüller, E. Bothe and K. Wieghardt, *Angew. Chem., Int. Ed.*, 2011, **50**, 1652–1655, (*Angew. Chem.*, 2011, **123**, 1690–1693); (*c*) F. Ehret, M. Bubrin, S. Záliš and W. Kaim, *Z. Anorg. Allg. Chem.*, 2014, **640**, 2781–2787.

5 A. Pariyar, G. Vijaykumar, M. Bhunia, S. K. Dey, S. K. Singh, S. Kurungot and S. K. Mandal, *J. Am. Chem. Soc.*, 2015, **137**, 5955–5960.

6 W. Kaim and G. K. Lahiri, *Angew. Chem., Int. Ed.*, 2007, **46**, 1778–1796, (*Angew. Chem.*, 2007, **119**, 1808–1828).

7 W. Kaim and B. Sarkar, *Coord. Chem. Rev.*, 2013, **257**, 1650–1659.

8 (*a*) P. Ghosh, R. Ray, A. Das and G. K. Lahiri, *Inorg. Chem.*, 2014, **53**, 10695–10707; (*b*) A. Das, S. M. Mobin and G. K. Lahiri, *Dalton Trans.*, 2015, **44**, 13204–13219; (*c*) A. Das, H. Agarwala, T. Kundu, P. Ghosh, S. Mondal, S. M. Mobin and G. K. Lahiri, *Dalton Trans.*, 2014, **43**, 13932–13947; (*d*) S. Ye, B. Sarkar, C. Duboc, J. Fiedler and W. Kaim, *Inorg. Chem.*, 2005, **44**, 2843–2847.

9 P. Majumdar, S.-M. Peng and S. Goswami, *J. Chem. Soc., Dalton Trans.*, 1998, 1569–1574.

10 (*a*) A. Das, T. Scherer, S. M. Mobin, W. Kaim and G. K. Lahiri, *Chem. – Eur. J.*, 2012, **18**, 11007–11018; (*b*) K. J. H. Young, O. A. Mironov, R. J. Nielsen, M.-J. Cheng, T. Stewart, W. A. Goddard and R. A. Periana, *Organometallics*, 2011, **30**, 5088–5094.

11 (*a*) A. Mandal, A. Grupp, B. Schwederski, W. Kaim and G. K. Lahiri, *Inorg. Chem.*, 2015, **54**, 10049–10057; (*b*) A. Das, P. Ghosh, S. Plebst, B. Schwederski, S. M. Mobin, W. Kaim and G. K. Lahiri, *Inorg. Chem.*, 2015, **54**, 3376–3386.

12 W. Kaim, *Coord. Chem. Rev.*, 1987, **76**, 187–235.
13 W. Kaim, *Chem. Ber.*, 1981, **114**, 3789–3800.
14 C. Wolff, A. Gottschlich, J. England, K. Wieghardt, W. Saak, D. Haase and R. Beckhaus, *Inorg. Chem.*, 2015, **54**, 4811–4820.
15 J. A. Weil, J. R. Bolton and J. E. Wertz, *Electron Paramagnetic Resonance*, Wiley, New York, 1994, p. 532–536.
16 M. Heilmann, F. Baumann, W. Kaim and J. Fiedler, *J. Chem. Soc., Faraday Trans.*, 1996, **92**, 4227–4231.
17 D. E. Morris, K. W. Hanck and M. K. DeArmond, *J. Am. Chem. Soc.*, 1983, **105**, 3032–3038.
18 S. Patra, B. Sarkar, S. M. Mobin, W. Kaim and G. K. Lahiri, *Inorg. Chem.*, 2003, **42**, 6469–6473.
19 D. Das, B. Sarkar, T. K. Mondal, S. M. Mobin, J. Fiedler, W. Kaim and G. K. Lahiri, *Inorg. Chem.*, 2011, **50**, 7090–7098.
20 (*a*) F. Ehret, M. Bubrin, S. Záliš and W. Kaim, *Angew. Chem., Int. Ed.*, 2013, **52**, 4673–4675, (*Angew. Chem.*, 2013, **125**, 4771–4773); (*b*) F. Ehret, M. Bubrin, S. Záliš and W. Kaim, *Chem. – Eur. J.*, 2015, **21**, 12275–12278.
21 J. Rall and W. Kaim, *J. Chem. Soc., Faraday Trans.*, 1994, **90**, 2905–2908.
22 N. Shaikh, S. Goswami, A. Panja, X.-Y. Wang, S. Gao, R. J. Butcher and P. Banerjee, *Inorg. Chem.*, 2004, **43**, 5908–5918.
23 W. Kaim, B. Schwederski and A. Klein, *Bioinorganic Chemistry: Inorganic Elements in the Chemistry of Life*, John Wiley & Son, Chichester, 2nd edn, 2013.
24 M. Krejcik, M. Danek and F. Hartl, *J. Electroanal. Chem.*, 1991, **317**, 179–187.
25 (*a*) P. S. Braterman, J.-I. Song, F. M. Wimmer, S. Wimmer, W. Kaim, A. Klein and R. D. Peacock, *Inorg. Chem.*, 1992, **31**, 5084–5088; (*b*) W. Kaim, R. Reinhardt and M. Sieger, *Inorg. Chem.*, 1994, **33**, 4453–4459.
26 W. Kaim, *Coord. Chem. Rev.*, 2011, **255**, 2503–2513.
27 C. Remenyi and M. Kaupp, *J. Am. Chem. Soc.*, 2005, **127**, 11399–11413.
28 P. A. Lay, M. Sargeson and H. Taube, *Inorg. Synth.*, 1986, **24**, 291–299.
29 B. K. Ghosh, S. Goswami and A. Chakravorty, *Inorg. Chem.*, 1983, **22**, 3358–3360.
30 R. C. Haddon, R. Rayford and A. M. Hirani, *J. Org. Chem.*, 1981, **46**, 4587–4588.
31 W. Kaim, S. Ernst and V. Kasack, *J. Am. Chem. Soc.*, 1990, **112**, 173–178.
32 S. Stoll and A. Schweiger, EasySpin, a comprehensive software package for spectral simulation and analysis in EPR, *J. Magn. Reson.*, 2006, **178**, 42–55.
33 (*a*) G. M. Sheldrick, *Acta Crystallogr., Sect. A: Fundam. Crystallogr*, 2008, **64**, 112–122; (*b*) *Program for Crystal Structure Solution and Refinement*, University of Goettingen, Goettingen, Germany, 1997.
34 M. J. Frisch, G. W. Trucks, H. B. Schlegel, G. E. Scuseria, M. A. Robb, J. R. Cheeseman, G. Scalmani, V. Barone, B. Mennucci, G. A. Petersson, H. Nakatsuji, M. Caricato, X. Li, H. P. Hratchian, A. F. Izmaylov, J. Bloino, G. Zheng, J. L. Sonnenberg, M. Hada, M. Ehara, K. Toyota, R. Fukuda, J. Hasegawa, M. Ishida, T. Nakajima, Y. Honda, O. Kitao, H. Nakai, T. Vreven, J. A. Montgomery, Jr., J. E. Peralta, F. Ogliaro, M. Bearpark, J. J. Heyd, E. Brothers, K. N. Kudin, V. N. Staroverov, R. Kobayashi, J. Normand, K. Raghavachari, A. Rendell, J. C. Burant, S. S. Iyengar, J. Tomasi, M. Cossi, N. Rega, J. M. Millam, M. Klene, J. E. Knox, J. B. Cross, V. Bakken, C. Adamo, J. Jaramillo, R. Gomperts, R. E. Stratmann, O. Yazyev, A. J. Austin, R. Cammi, C. Pomelli, J. W. Ochterski, R. L. Martin, K. Morokuma, V. G. Zakrzewski, G. A. Voth, P. Salvador, J. J. Dannenberg, S. Dapprich, A. D. Daniels, O. Farkas, J. B. Foresman, J. V. Ortiz, J. Cioslowski and D. J. Fox, *Gaussian 09 (Revision A.02)*, Gaussian, Inc., Wallingford, CT, 2009.
35 ADF2016.01, *SCM, Theoretical Chemistry*, Vrije Universiteit, Amsterdam, The Netherlands, http://www.scm.com.
36 (*a*) J. P. Perdew, K. Burke and M. Ernzerhof, *Phys. Rev. Lett.*, 1996, **77**, 3865–3868; (*b*) C. Adamo and V. Barone, *J. Chem. Phys.*, 1999, **110**, 6158–6170.
37 (*a*) D. Andrae, U. Haeussermann, M. Dolg, H. Stoll and H. Preuss, *Theor. Chim. Acta*, 1990, **77**, 123–141; (*b*) P. Fuentealba, H. Preuss, H. Stoll and L. von Szentpaly, *Chem. Phys. Lett.*, 1989, **89**, 418–422; (*c*) J. M. L. Martin and A. Sundermann, *J. Chem. Phys.*, 2001, **114**, 3408.
38 K. Raghavachari, J. S. Binkley, R. Seeger and J. A. Pople, *J. Chem. Phys.*, 1980, **72**, 650–654.
39 C. Lee, W. Yang and R. G. Parr, *Phys. Rev. B: Condens. Matter*, 1988, **37**, 785–789.
40 (*a*) R. Bauernschmitt and R. Ahlrichs, *Chem. Phys. Lett.*, 1996, **256**, 454–464; (*b*) R. E. Stratmann, G. E. Scuseria and M. J. Frisch, *J. Chem. Phys.*, 1998, **109**, 8218–8225; (*c*) M. E. Casida, C. Jamorski, K. C. Casida and D. R. Salahub, *J. Chem. Phys.*, 1998, **108**, 4439–4450.
41 (*a*) V. Barone and M. Cossi, *J. Phys. Chem. A*, 1998, **102**, 1995–2001; (*b*) M. Cossi and V. Barone, *J. Chem. Phys.*, 2001, **115**, 4708–4718; (*c*) M. Cossi, N. Rega, G. Scalmani and V. Barone, *J. Comput. Chem.*, 2003, **24**, 669–681.
42 E. V. Lenthe, A. E. Ehlers and E. J. Baerends, *J. Chem. Phys.*, 1999, **110**, 8943–8953.
43 E. V. Lenthe, E. J. Baerends and J. G. Snijders, *J. Chem. Phys.*, 1993, **99**, 4597–4610.
44 (*a*) E. V. Lenthe, A. van der Avoird and P. E. S. Wormer, *J. Chem. Phys.*, 1997, **107**, 2488; (*b*) E. V. Lenthe, A. van der Avoird and P. E. S. Wormer, *J. Chem. Phys.*, 1998, **108**, 4783.
45 S. Leonid, *Chemissian 1.7*, 2005–2010. Available at http://www.chemissian.com.
46 D. A. Zhurko and G. A. Zhurko, *ChemCraft 1.5*, Plimus, San Diego, CA. Available at http://www.chemcraftprog.com.